Graphene-Supported Nickel Ferrite: A Magnetically Separable Photocatalyst with High Activity under Visible Light

Yongsheng Fu
Key Laboratory of Soft Chemistry and Functional Materials, Nanjing University of Science and Technology, Ministry of Education, Nanjing 210094, China, and Key Laboratory of Fine Petrochemical Engineering, Changzhou University, Changzhou 213164, China,

Haiqun Chen and Xiaoqiang Sun
Key Laboratory of Fine Petrochemical Engineering, Changzhou University, Changzhou 213164, China

Xin Wang
Key Laboratory of Soft Chemistry and Functional Materials, Nanjing University of Science and Technology, Ministry of Education, Nanjing 210094, China, and Key Laboratory of Jiangsu Province for Chemical Pollution Control and Resources Reuse, Nanjing University of Science and Technology, Nanjing 210094, China

DOI 10.1002/aic.13716
Published online December 22, 2011 in Wiley Online Library (wileyonlinelibrary.com).

A straightforward strategy is designed for the fabrication of a magnetically separable $NiFe_2O_4$-graphene photocatalyst with different graphene content. It is very interesting that the combination of $NiFe_2O_4$ nanoparticles with graphene sheets results in a dramatic conversion of the inert $NiFe_2O_4$ into a highly active catalyst for the degradation of methylene blue (MB) under visible light irradiation. The significant enhancement in photoactivity under visible light irradiation can be ascribed to the reduction of GO, because the photogenerated electrons of $NiFe_2O_4$ can transfer easily from the conduction band to the reduced GO, effectively preventing a direct recombination of electrons and holes. The results of the kinetic study indicated that the rate-determining stage is the adsorption process of MB molecules. $NiFe_2O_4$ nanoparticles themselves have a strong magnetic property, which can be used for magnetic separation in a suspension system, and, therefore, the introduction of additional magnetic supports is no longer necessary. © 2011 American Institute of Chemical Engineers
AIChE J, 58: 3298–3305, 2012
Keywords: $NiFe_2O_4$-graphene, photocatalyst, magnetic separation, visible light irradiation, radicals' oxidation reaction

Introduction

In recent years, photocatalytic technology, especially TiO_2 photocatalysis, has been extensively used for the treatment of polluted water. However, the effective photoexcitation of TiO_2 photocatalysts requires the application of light with energy higher than its band-gap energy of 3.2 eV, implying the photodegradation only occurs under UV irradiation. Since the UV region occupies only near 4% of the entire solar spectrum, while 45% of the energy belongs to visible light, most solar energy cannot be used. Therefore, developing efficient visible-light-driven photocatalysts for environmental remediation has become an active area in photocatalysis research, including dye sensitization, external surface modifications and band gap tailoring.[1–7]

Since its discovery in 2004, graphene has attracted extraordinary interest for fundamental studies, as well as for potential applications.[8–11] As a new carbon material, graphene possesses single-atom thickness, a two-dimensional (2-D) conjugated structure, and exceptional physical and chemical properties.[12–16] It has been receiving recent attention as a support for catalysts. Some recent efforts have been made to fabricate graphene-metal oxide photocatalysts, such as TiO_2-graphene and ZnO-graphene, for photodegration of organic molecules under UV irradiation.[12,17–22]

Photodegradation reactions are usually carried out in heterogeneous systems. Recovery and reuse of photocatalysts after degradation are of great importance for sustainable process management. The introduction of magnetic nanoparticles in a variety of solid matrices allows the combination of well-known procedures for catalyst heterogenization with techniques for magnetic separation.[23]

Nickel ferrite ($NiFe_2O_4$) with an inverse spinel structure shows ferrimagnetism that originates from a magnetic moment of antiparrallel spins between Fe^{3+} ions at tetrahedral sites and Ni^{2+} ions at octahedral sites.[24] This ferrite is one of the most important magnetic materials having high-electrical resistivity, high-Curie temperature and environmental stability. Magnetic nanoparticles of nickel ferrite have been used to fabricate titania-coated nickel ferrite, which is a magnetically separable photocatalyst.[25] Although $NiFe_2O_4$ has a band gap of 2.19 eV,[26] to the best of our knowledge, little research has been conducted on its photocatalytic activity under visible

Additional Supporting Information can be found in the online version of this article.

Correspondence concerning this article should be addressed to X. Wang at wxin@public1.ptt.js.cn.

© 2011 American Institute of Chemical Engineers

light irradiation. Indeed, as will be seen later, pure nickel ferrite is a photocatalytically inert compound. Even though, if $NiFe_2O_4$ nanoparticles are coupled with another semiconductor (e.g., graphene sheets), it is possible to improve the efficiency of photoinduced charge separation, leading to high-photocatalytic performance.

In a recent report, we have addressed the fabrication of a $ZnFe_2O_4$-graphene photocatalyst and its high performance in the photocatalytic degradation of MB in the presence of hydrogen peroxide under visible light irradiation.[27] It is well-known that hydrogen peroxide is manufactured by a process that consumes energy, and/or other chemical resources. Therefore, it is of great interest to design magnetically separable graphene-based photocatalysts having high-catalytic activity in the absence of hydrogen peroxide.

Herein, a straightforward strategy is designed to deposit $NiFe_2O_4$ nanocrystals on graphene sheets via a one-step hydrothermal method. Interestingly, in the presence of graphene the inert nanocrystals of $NiFe_2O_4$ have been dramatically converted into a highly active catalyst for the degradation of methylene blue (MB) under visible light irradiation in the absence of hydrogen peroxide. In addition, $NiFe_2O_4$ nanoparticles themselves have a magnetic property, which makes the $NiFe_2O_4$-graphene composite magnetically separable in a suspension system, and, therefore, it does not require additional magnetic components as is the usual case.

Experimental

Synthesis of magnetic $NiFe_2O_4$-graphene composite photocatalyst

Graphene oxide (GO) was synthesized from purified natural graphite bought from Qingdao Zhongtian, Co., with a mean particle size of 44 μm according to the method reported by Hummers and Offeman.[28] $NiFe_2O_4$-graphene nanocomposite photocatalysts with different graphene content (0.5, 1, 3, 5, 10, 15, 20, 25, 30, 40 wt %) were synthesized. A typical experiment for the synthesis of $NiFe_2O_4$-graphene nanocomposite with 25% graphene content is as follows: 80 mg of GO was dispersed into 60 mL of absolute ethanol with sonication for 1 h. Then 0.291 g of $Ni(NO_3)_2{\cdot}6H_2O$ and 0.8080 g of $Fe(NO_3)_3{\cdot}9H_2O$ were added to 20 mL of absolute ethanol with stirring for 30 min at room temperature. The aforementioned two systems were then mixed together, and stirred for 30 min. Then the mixture was adjusted to a pH of 10.0 with 6M NaOH solution, and stirred for 30 min, yielding a stable bottle-green homogeneous emulsion. The resulting mixture was transferred into a 100 mL Teflon-lined stainless steel autoclave and heated to 180°C for 20 h under autogenous pressure. The reaction mixture was allowed to cool to room temperature and the precipitate was filtered, washed with distilled water five times, and dried in a vacuum oven at 60°C for 12 h. The product was labeled as $NiFe_2O_4$-G(0.25). For comparison, same method was used to synthesize pure $NiFe_2O_4$ without GO.

Characterization

Fourier transform infrared (FTIR) spectra were recorded on a Bruker VECTOR 22 spectrometer using the KBr pellet technique. X-ray photoelectron spectra (XPS) were carried out on a RBD upgraded PHI-5000C ESCA system (PerkinElmer) with Mg Kα radiation ($h\nu$ = 1253.6 eV). Raman spectra were acquired on a Renishaw inVia Reflex Raman Microprobe. Powder X-ray diffraction (XRD) analyses were performed on a Bruker D8 advanced diffractometer with Cu Ka radiation and the scanning angle ranged from 5 to 70° of 2θ. Transmission electron microscopy (TEM) images were taken with a JEOL JEM2100 microscope. Photoluminescence spectra were recorded on a Jobin Yvon SPEX Fluorolog-3-P spectroscope, and a 450 W Xe lamp was used as the excitation source.

Electrochemical impedance spectroscopy (EIS) measurements were performed with a CHI660B workstation. The test electrodes were prepared according to the Ref. 29. EIS measurements were carried out in 1 M H_2SO_4 by using a three-electrode system, with a platinum foil electrode as the counterelectrode and a saturated calomel electrode (SCE) as the reference electrode. EIS measurements were recorded with an AC voltage amplitude of 5 mV, with a frequency range of 1 MHz to 5 mHz at 0.5 V.

Photocatalytic activity measurement

The photocatalytic activity of the prepared samples was determined by the degradation of MB under visible light irradiation. Photoirradiation was carried out using a 500 W xenon lamp through UV cutoff filters (JB450) to completely remove any radiation below 420 nm and to ensure illumination by visible-light only. Experiments were conducted at 25°C as follows: 0.025 g of photocatalyst was added to 100 mL of a 20 mg/L dye aqueous solution. Before starting the illumination, the reaction mixture was stirred for 60 min in the dark in order to reach the adsorption-desorption equilibrium between the dye and the catalyst. At a given time interval of irradiation, 5 mL aliquots were withdrawn, and then magnetically separated to remove essentially all the catalyst. The concentrations of the remnant dye were spectrophotometrically monitored by measuring the absorbance of solutions at 664 nm during the photodegradation process. After photocatalytic reactions on the $NiFe_2O_4$-G(0.25) system, the aqueous solution was analyzed using ion chromatography system (Dionex ICS-90).

Photocurrent was measured on a CHI 660B electrochemical workstation in a standard three-electrode system using the prepared samples as the working electrodes with an active area of about 0.5 cm^2. Platinum foil and a saturated calomel electrode (SCE) were used as the counter and reference electrodes, respectively. A 500 W xenon lamp with a 420 nm cutoff filter (the average light intensity was 31.2 $mWcm^{-2}$) was used as the source of visible light irradiation.

Results and Discussion

Structure and morphology of $NiFe_2O_4$-graphene nanocomposite photocatalyst

The XRD diffraction patterns of the as-prepared $NiFe_2O_4$-graphene nanocomposites, pure $NiFe_2O_4$, reduced graphene oxide and GO are shown in Figure 1A. It can be seen that almost all the diffraction peaks of $NiFe_2O_4$-graphene may be assigned to spinel-type $NiFe_2O_4$ (JCPDS 54-0964). The peaks at the 2θ values of 18.3, 30.1, 35.3, 43.0, 53.5, 56.3, and 62.4° can be indexed to (111), (220), (311), (400), (422), (511) and (440) crystal planes of spinel $NiFe_2O_4$, respectively. However, no typical diffraction peak of graphite (002) or GO (001) is observable in the XRD pattern for $NiFe_2O_4$-graphene. This may be ascribed to the fact that during the hydrothermal reaction, crystal growth of $NiFe_2O_4$ between the interlayer of GO destroyed the regular layer stacking, leading to the exfoliation of GO and the disappearance of the (001) diffraction peak. On the other hand,

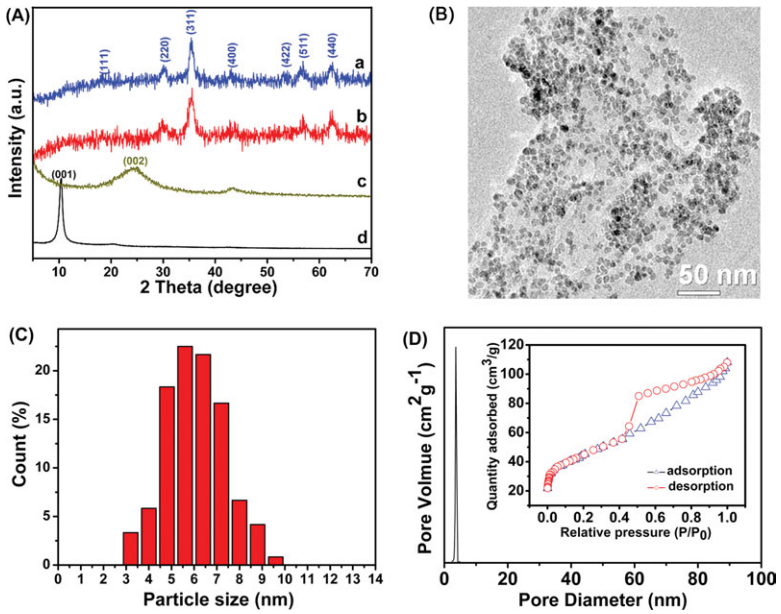

Figure 1. (A) XRD patterns of (a) $NiFe_2O_4$-G(0.25), (b) pure $NiFe_2O_4$, (c) reduced graphene oxide, and (d) graphite oxide (GO) in the range of 5–70°; (B) Typical TEM image of $NiFe_2O_4$-G(0.25); (C) The particle size distribution for $NiFe_2O_4$; (D) N_2-sorption isotherms (inset) and corresponding pore-size distribution curves for $NiFe_2O_4$-G(0.25).

[Color figure can be viewed in the online issue, which is available at wileyonlinelibrary.com.]

graphene oxide sheets can be reduced under the hydrothermal conditions in the presence of alcohols, and the exfoliated reduced GO sheets show no peak of (002). As shown in Figure 1S (see online in Supplementary materials), the intensity of diffraction peaks for the composites varies inversely with the graphene content.

The morphology of as-obtained $NiFe_2O_4$-graphene nanocomposite was investigated by TEM. As can be seen from Figure 1B, the almost transparent graphene sheets are fully exfoliated and decorated with $NiFe_2O_4$ nanocrystals having an average diameter of 6.05 nm and a narrow particle-size distribution (Figure 1C). Figure 1D gives the nitrogen adsorption-desorption isotherms (inset), and pore-size distribution plots for the $NiFe_2O_4$-G(0.25). The isotherm shows a typical IUPAC type IV pattern, implying the existence of mesopores. The measurements indicate that the sample has a Brunauer-Emmett-Teller (BET, nitrogen, 77 K) surface area of 135.37 $m^2 \cdot g^{-1}$. The BJH desorption average pore diameter is 3.73 nm with very narrow pore-size distribution, and pore volume is 0.1218 $m^2 \cdot g^{-1}$.

It is known that graphene can be obtained by removal of the oxygen from graphene oxide sheets via hydrothermal reaction in the presence of reducing agents.[17,19] The XPS results showed a decrease in oxygen content in $NiFe_2O_4$-G(0.25) compared with GO (see Table 1S in Supplementary materials). As shown in Figure 2A and 2B, the intensity of some oxygen-containing groups on carbon sheets in the as-prepared composite was obviously reduced, indicating the deoxygenation of graphene oxide. Especially, the epoxy groups were considerably reduced on the carbon sheets in the composite compared with the starting graphite oxide. This indicates that GO has been reduced to graphene with a small amount of residual oxygen-containing groups via hydrothermal reaction. Figure 2S (see Supplementary materials) displays the typical Ni 2p and Fe 2p XPS spectra of $NiFe_2O_4$-G(0.25), which is in agreement with published work on $NiFe_2O_4$ particles.[30] The reduction of GO in $NiFe_2O_4$-graphene was also examined by FTIR spectroscopy (Figure 2C). It can be clearly seen that almost all the characteristic peaks of oxygen-containing groups (C=O, O—H, C—OH and C—O—C) disappeared for $NiFe_2O_4$-G(0.25), suggesting that GO in the composite has been reduced to graphene. The adsorption of $NiFe_2O_4$-G(0.25) around 1,570 cm^{-1} may be assigned to the stretching vibrations of the unoxidized carbon backbone.[31–33] The two strong absorption peaks at lower frequencies (ca. 550 and 415 cm^{-1}) can be assigned to the stretching vibrations of the Ni—O bonds in tetrahedral positions and the Fe—O bonds in octahedral positions, respectively.[30,34,35]

Raman spectroscopy is one of the most sensitive and informative techniques to characterize disorder in sp^2 carbon materials. As shown in Figure 2D, for $NiFe_2O_4$-G(0.25), Raman peaks of G- and D-bands shift to lower frequency in comparison with that of GO: the G-band shifted from 1602 to 1599 cm^{-1}, whereas the D-band shifted from 1,360 to 1,330 cm^{-1}, indicating that GO has been reduced to graphene. Besides, the two-dimensional (2-D) band at 2,694 cm^{-1} is also seen, which is further indicative of the reduction of GO and the formation of graphene structure. The peak position of the 2-D band is similar to that of a monolayer graphene,[36–39] and this result can be confirmed by atomic force microscopy (AFM) image of $NiFe_2O_4$-G(0.25) in Figure 3S (see Supplementary materials). The two Raman spectra of $NiFe_2O_4$-G(0.25) and pure $NiFe_2O_4$ show similar features in the range of 100–1000 cm^{-1}, and this is in agreement with published work on $NiFe_2O_4$ particles.[40,41] Figure 4S (see Supplementary materials) shows the Raman spectra of the $NiFe_2O_4$-graphene nanocomposites with different graphene content. It is obvious that the intensity ratio of the D- to G-band ($I_{D\text{-band}}/I_{G\text{-band}}$) decreases with increasing graphene content in the $NiFe_2O_4$-graphene nanocomposites, indicative of the increase of degree of graphitization and the existence of graphene in the $NiFe_2O_4$-graphene nanocomposites.

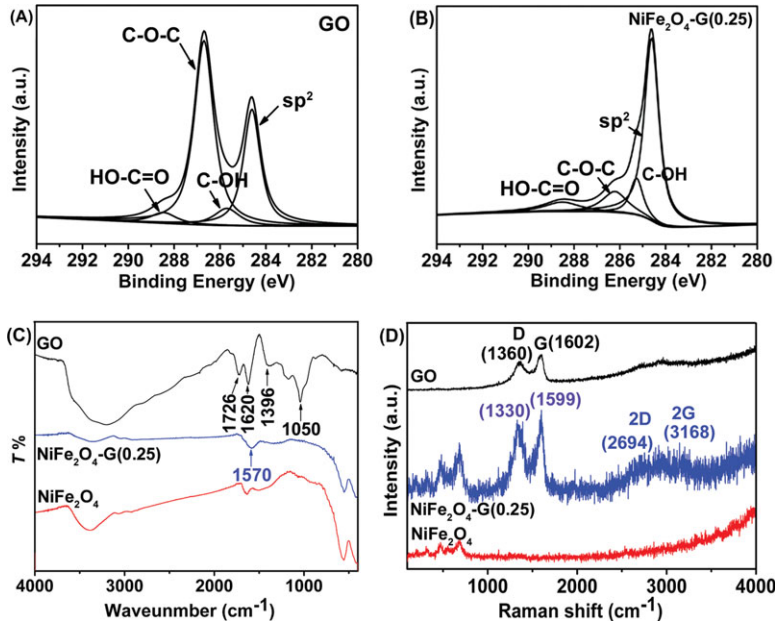

Figure 2. (A) C1 s XPS spectra of GO; (B) C1 s XPS spectra of $NiFe_2O_4$-G(0.25); (C) FTIR spectra, and (D) raman spectra of GO, $NiFe_2O_4$—G(0.25) and pure $NiFe_2O_4$.

[Color figure can be viewed in the online issue, which is available at wileyonlinelibrary.com.]

Optical absorption properties of photocatalysts are very important in the photocatalysis process. Figure 5S (Supplementary materials) displays the UV–vis diffuse reflectance spectra of pure $NiFe_2O_4$ and $NiFe_2O_4$-graphene photocatalyst with different graphene content. For the $NiFe_2O_4$-G(0.005) and $NiFe_2O_4$-G(0.01), there is an obvious redshift at the absorption edge compared to pure $NiFe_2O_4$, implying a narrowing in the band gap of $NiFe_2O_4$ due to the presence of graphene. When the content of graphene in the nanocomposite photocatalyst is above 3%, the absorption of the $NiFe_2O_4$-graphene system is so strong that the absorption edge cannot be observed.

Photocatalytic properties and reaction kinetics

The photocatalytic activities of the as-obtained $NiFe_2O_4$-graphene nanocomposite photocatalysts with different graphene content were evaluated by the degradation of methylene blue (MB) under visible-light irradiation at 25°C. Figure 3A shows the changes in the absorbance profiles of MB solution in the presence of $NiFe_2O_4$-G(0.25) photocatalyst under visible-light irradiation at 25°C. The adsorption-desorption equilibrium solution of MB and $NiFe_2O_4$-G(0.25) was used as starting solution (the spectrum is shown in Figure 3A), $t = 0$ min). It can be clearly seen that almost all the MB molecules in the solution were decomposed after 180 min. As indicated in the introduction section $NiFe_2O_4$, as a soft magnetic material, possesses remarkable magnetic properties, which gives it good performance in magnetic separation for the $NiFe_2O_4$-graphene photocatalysts using an external magnet (see the inset of Figure 3A and online in Supplementary materials (video)).

Figure 3B shows time profiles of C/C_0 using different photocatalysts under visible light irradiation at 25°C, where C is the concentration of MB at the irradiation time t and C_0 is the concentration of the adsorption-desorption equilibrium solution of MB and $NiFe_2O_4$-G(0.25) before irradiation ($t = 0$ min). It is very interesting that $NiFe_2O_4$, GO or reduced GO alone is a photocatalytically inert compound photocatalytic activity under visible light irradiation (Figure 3B (a) and Figure 6S (see Supplimentary materials)), while the combonation of $NiFe_2O_4$ nanoparticles with reduced

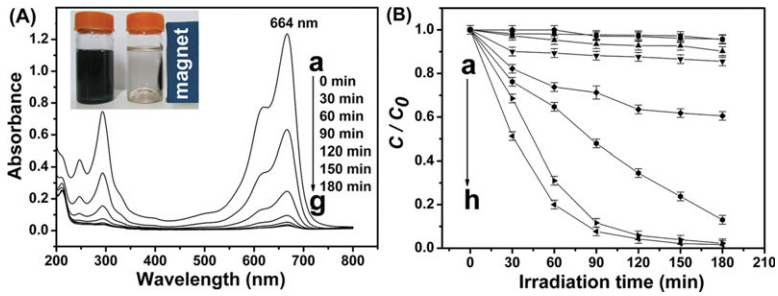

Figure 3. (A) Absorption spectra of the MB solution taken at different photocatalytic degradation times using $NiFe_2O_4$-G(0.25).

The inset reveals the magnetic separation property of $NiFe_2O_4$-graphene nanocomposite; (B) Effect of different catalysts on photocatalytic degradation of MB: (a) pure $NiFe_2O_4$, (b) $NiFe_2O_4$-G(0.05), (c) $NiFe_2O_4$-G(0.10), (d) $NiFe_2O_4$-G(0.15), (e) $NiFe_2O_4$-G(0.20), (f) $NiFe_2O_4$-G(0.40), (g)$NiFe_2O_4$-G(0.30), and (h) $NiFe_2O_4$-G(0.25). [Color figure can be viewed in the online issue, which is available at wileyonlinelibrary.com.]

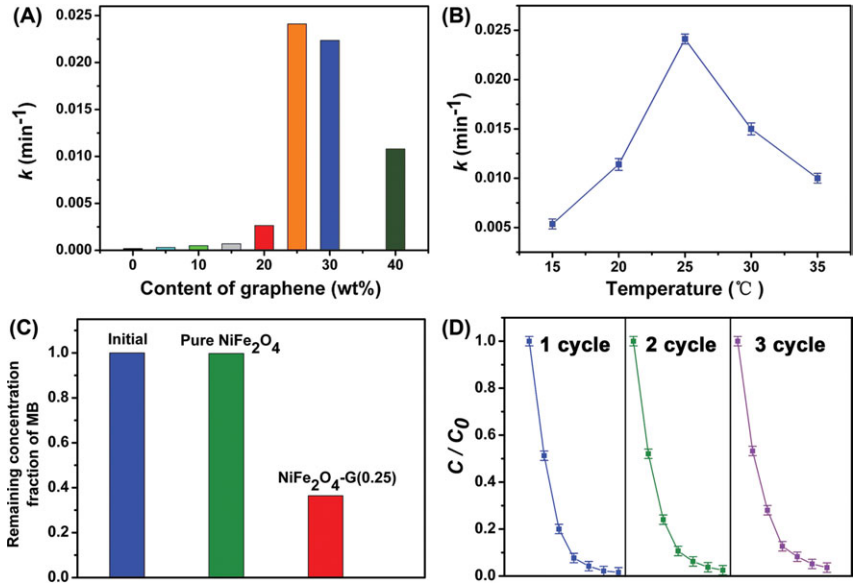

Figure 4. The rate constant for the photodecomposition of MB (A) on $NiFe_2O_4$-graphene photocatalysts with different graphene content, (B) on $NiFe_2O_4$-G(0.25) photocatalysts at different temperatures, (C) bar plot showing the remaining MB in solution after reaching the adsorption-desorption equilibrium in the dark for 60 min with stirring, and (D) the photodegradation rate of MB in solution for 3 cycles using $NiFe_2O_4$-G(0.25) photocatalyst.

[Color figure can be viewed in the online issue, which is available at wileyonlinelibrary.com.]

graphene results in a dramatic conversion (Figure 3B (f-h)). With increasing graphene content in $NiFe_2O_4$-graphene photocatalyst, faster MB degradation was observed, and 25% (w/w) graphene in $NiFe_2O_4$-graphene gave the best performance in photocatalytic activity (Figure 3B (h)).

It is well recognized that the photocatalytic degradation of MB follows a pseudo-first-order kinetics behavior. The rate constant (k) can be calculated for the photocatalytic degradation of MB under visible-light irradiation at 25°C according to Eq. 1

$$k = \frac{1}{t}\ln\frac{c}{c_0} \tag{1}$$

where C_0 and C are the concentration of MB when reaction time is 0 and t, respectively.

Figure 4A shows the values for the pseudo-first-order rate constant (k) for the photodecomposition of MB by $NiFe_2O_4$-graphene photocatalysts with different graphene content. Among these catalysts, $NiFe_2O_4$-G(0.25) showed the best photocatalytic activity ($k = 0.02421\ min^{-1}$). In contrast, $NiFe_2O_4$-graphene with lower graphene content (<20%) gave poorer activity, and pure $NiFe_2O_4$ showed no photocatalytic activity at all.

The influence of temperature on the rate constant (k) was also monitored and the results are shown in Figure 4B. It can be seen that the rate constant (k) first increased and then decreased with rising temperatures. It reached a maximum value at $0.02421\ min^{-1}$ at 25°C. It is known that the preliminary adsorption of MB on the $CoFe_2O_4$-graphene photocatalyst surface is a prerequisite for highly efficient photooxidation.[42,43] Figure 4C displays the remaining solution of MB after reaching the adsorption-desorption equilibrium in the dark with the pure $NiFe_2O_4$ and with $NiFe_2O_4$-G(0.25). It can be clearly seen that a large amount of dye molecules (ca. 65%) was adsorbed on the surface of $NiFe_2O_4$-G(0.25). The enhanced adsorptivity should be largely assigned to larger surface area of $NiFe_2O_4$-G(0.25), which can offer more active adsorption sites and photocatalytic reaction centers, and the π-π stacking and/or electrostatic attraction between MB and π-conjugation regions of the graphene sheets.[17]

The photocatalytic activity of the recycled $NiFe_2O_4$-G(0.25) catalyst was also investigated, and the results are shown in Figure 4D. There was no noticeable change in the photocatalytic activity of the recycled catalyst after three cycles under visible light irradiation, indicating that the magnetically separable photocatalyst $NiFe_2O_4$-G(0.25) is stable and effective for the degradation of organic pollutants in water.

Mechanism of photocatalytic activity enhancement

As indicated earlier, $NiFe_2O_4$-G(0.25) gave the best photocatalytic activity for MB degradation. The significant enhancement in photoactivity under visible light irradiation can be ascribed to the remarkable synergistic effect between $NiFe_2O_4$ and the graphene sheets, leading to the efficient separation of photogenerated carriers in the $NiFe_2O_4$ and graphene coupling system. A possible mechanism of photocatalytic activity enhancement is proposed as follows

$$NiFe_2O_4 + h\nu \rightarrow NiFe_2O_4(h + e) \tag{1}$$

$$NiFe_2O_4(e) + \text{graphene} \rightarrow NiFe_2O_4 + \text{graphene}(e) \tag{2}$$

$$\text{graphene}(e) + O_2 \rightarrow O_2^{\cdot-} + \text{graphene} \tag{3}$$

$$NiFe_2O_4(h) + OH^- \rightarrow NiFe_2O_4 + \cdot OH \tag{4}$$

$$NiFe_2O_4(h) + \cdot OH + O_2^{\cdot-} + MB \rightarrow CO_2 + H_2O + SO_4^{2-} + NO_3^- + Cl^- + NH_4^+ \tag{5}$$

Upon visible-light excitation, the electron-hole pairs are generated on the $NiFe_2O_4$ surface (Reaction 1), followed by

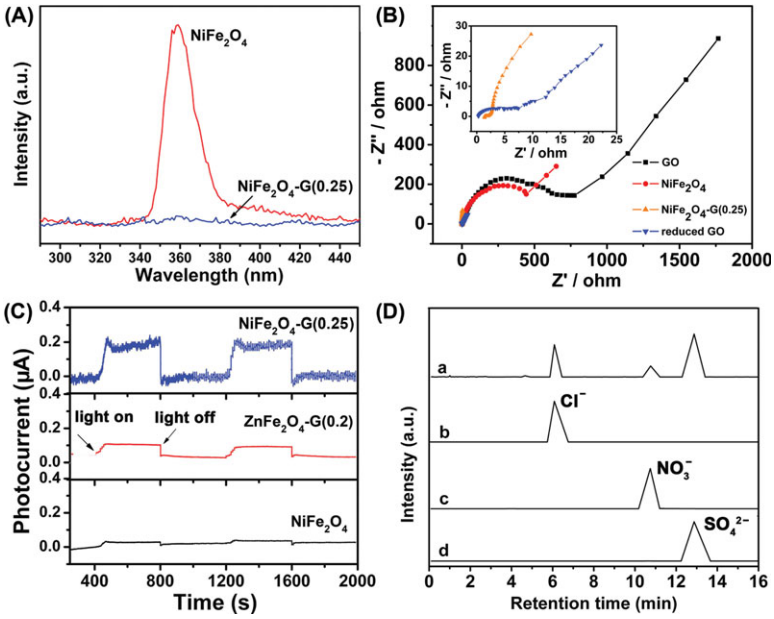

Figure 5. (A) The room-temperature photoluminescence (PL) spectra of pure $NiFe_2O_4$ and $NiFe_2O_4$-G(0.25) (λex = 270 nm), (B) The electrochemical impedance spectra (EIS) of $NiFe_2O_4$-G(0.25), pure $NiFe_2O_4$, GO and reduced GO.

The spectrum in the inset is enlarged to show the impedance of $NiFe_2O_4$-G(0.25) and reduced GO, (C) photocurrent transient responses of pure $NiFe_2O_4$, $ZnFe_2O_4$-G(0.2) and $NiFe_2O_4$-G(0.25) electrodes under visible-light irradiation, [Na_2SO_4] = 0.5M, and (D) ion chromatography analysis of (a) the solution after the photocatalytic reactions on the $NiFe_2O_4$—G(0.25) system, (b) sodium chloride standard solution, (c) sodium nitrate standard solutionand, and (d) sodium sulfate standard solution (eluent: 20 mM KOH; flow Rate: 1.0 mL/min; applied current: 75 Ma; injection volume: 10 μL; detection: duppressed conductivity). [Color figure can be viewed in the online issue, which is available at wileyonlinelibrary.com.]

instant transfer of photogenerated electrons onto graphene sheets via a percolation mechanism (Reaction 2), and then the negatively charged graphene sheets can activate the dissolved oxygen to produce superoxide anion radical (Reaction 3), while the holes can react with the adsorbed water to form hydroxyl radical (Reaction 4). Finally, the active species (holes, superoxide anion radical and hydroxyl radical) oxidize the MB molecules adsorbed on the active sites of the $NiFe_2O_4$-graphene system through the π-π stacking and/or electrostatic attraction (Reaction 5).

To analyze the synergistic effect between $NiFe_2O_4$ and graphene, the measurements of the PL spectra were performed to disclose the migration, transfer, and recombination processes of the photogenerated electron-hole pairs. Figure 5A displays PL emission spectra of pure $NiFe_2O_4$ and $NiFe_2O_4$-G(0.25) photocatalyst monitored at an excitation wavelength of 270 nm. It can be seen that the emission of pure $NiFe_2O_4$ is centered at 360 nm, which is attributed to the recombination of holes and electrons in the valence band and conduction band. The $NiFe_2O_4$-G(0.25) heteroarchitecture exhibited a much lower emission intensity than pure $NiFe_2O_4$, implying that the recombination of photogenerated electrons and holes is inhibited greatly in the $NiFe_2O_4$-G(0.25) system. Because of their efficient electron-transport property, graphene sheets can significantly quench the fluorescence of $NiFe_2O_4$ anchored on them. The photogenerated electrons of excited $NiFe_2O_4$ were transferred instantly from the conduction band of $NiFe_2O_4$ to graphene via a percolation mechanism, resulting in an improved and efficient charge separation and offering much enhanced photocatalytic activity.[5,44]

The synergistic effect between $NiFe_2O_4$ and graphene can be further examined by the electrochemical impedance technique which is a reliable way to characterize electrical conductivity. As shown in Figure 5B, the impedance plot of $NiFe_2O_4$-G(0.25) involves an extremely small radius, much smaller than those of GO and pure $NiFe_2O_4$ electrodes. A large decrease in charge-transfer resistance of $NiFe_2O_4$-G(0.25) is definitely due to the reduction of GO in the hydrothermal reaction process. To a great extent, the significant enhancement of photocatalytic activity is ascribed to the reduction of GO since the photogenerated electrons of $NiFe_2O_4$ can transfer easily from the conduction band to the reduced GO which has superior electrical conductivity (the inset of Figure 5B), effectively preventing a direct recombination of electrons and holes.

To give further evidence to investigate the synergistic effect between nanoparticles and graphene sheets, the transient photocurrent responses of pure $NiFe_2O_4$, $ZnFe_2O_4$-G(0.2) and $NiFe_2O_4$-G(0.25) electrodes were recorded via several on-off cycles of irradiation. Figure 5C shows the photocurrent transient responses under visible light and dark for these samples where the photocurrent was measured at 0.0 V vs. SCE in 0.5 M Na_2SO_4 aqueous solution. The photocurrent of the $NiFe_2O_4$-G(0.25) electrode (0.2 μA) was about 13 times as high as that of the $NiFe_2O_4$ electrode (0.015 μA), indicating that the separation efficiency of photoinduced electrons and holes was much improved as a result of the electronic interaction between $NiFe_2O_4$ nanoparticles and graphene sheets. It can also be noted that the $ZnFe_2O_4$-G(0.2) electrode only gave a photocurrent response of 0.05 μA, much smaller than that of $NiFe_2O_4$-G(0.25), and this may explain why $ZnFe_2O_4$-G(0.2) can show a high-photocatalytic activity only in the presence of hydrogen peroxide.[27]

To understand the photocatalytic mechanism, the main active oxidant in the photocatalytic reaction process should be identified. It is well-known that the oxidants generated in the photocatalytic process can be measured through trapping

by *tert*-butyl alcohol (t-BuOH) and disodium ethylenediamine tetraacetate (EDTA-2Na).[22] It can be clearly seen from Figure 7S (Supplementary materials) that the addition of t-BuOH greatly reduces the photodegradation rate of MB in the $NiFe_2O_4$-G(0.25) suspension. In contrast, the addition of EDTA-Na has little effect on the photodegradation rate of MB. This implies that most of the holes react with the adsorbed water to produce OH radicals, and only a few of them can directly oxidize MB molecules. Therefore, we can conclude that OH radicals play the role of the main oxidant in the $NiFe_2O_4$-G(0.25) system and the radicals' oxidation reaction is obviously dominant.

It can be seen that there are three observable peaks to SO_4^{2-}, NO_3^-, and Cl^- ions in the chromatogram (Figure 5D). The stong peak of SO_4^{2-} indicated the sulfur atoms were completely oxidized to SO_4^{2-} ions, and the relatively weak signal of NO_3^- indicated that only a part of nitrogen atoms were oxidized to NO_3^-, implying NH_4^+ was the main product of nitrogen transformation for the photodegradation.[45]

Conclusions

In conclusion, a magnetically separable $NiFe_2O_4$-graphene photocatalyst with different graphene content has been successfully prepared via a one-step hydrothermal method. TEM observations indicate that graphene sheets are fully exfoliated and decorated with $NiFe_2O_4$ nanocrystals having an average diameter of 6.05 nm and a narrow particle-size distribution. The photocatalytic activity measurements demonstrate that the combination of $NiFe_2O_4$ nanoparticles with graphene sheets results in a dramatic conversion of the inert $NiFe_2O_4$ into a highly active catalyst for the degradation of methylene blue (MB) under visible light irradiation. The significant enhancement in photoactivity can be ascribed to the reduction of GO, as the excellent conductivity of the reduced GO sheets is favorable for the efficient separation of photogenerated carriers in the $NiFe_2O_4$ and graphene coupling system. It was found that the hydroxyl radical oxidation reaction was obviously dominant in the photodegradation process. Finally, it should be pointed out that there are very large and useful changes in photocatalytic activity after coupling nickel ferrite with graphene sheets, however, much more remains to be done, especially when considering the practical application of these graphene supported magneitc semiconductors in visible-light-sensitive photocatalysts for organic pollution degradation and water splitting.

Acknowledgments

This investigation was supported by the National Natural Science Foundation of China (No. 21171094), A Project Funded by the Priority Academic Program Development of Jiangsu Higher Education Institutions, NUST Research Funding (2011PYXM03) and the Dept. of Education of Jiangsu Province (CXZZ11_0245).

Literature Cited

1. Hoffmann MR, Martin ST, Choi W, Bahnemann DW. Environmental applications of semiconductor photocatalysis. *Chem Rev*. 1995; 95:69–96.
2. Mahrov B, Boschloo G, Hagfeldt A, Dloczik L, Dittrich T. Photovoltage study of charge injection from dye molecules into transparent hole and electron conductors. *Appl Phys Lett*. 2004;84: 5455–5457.
3. Hattori A, Tokihisa Y, Tada H, Ito S. Acceleration of oxidations and retardation of reductions in photocatalysis of a TiO_2/SnO_2 bilayer-type catalyst. *J Electrochem Soc*. 2000;147:2279–2283.
4. Ropidas GK, Bohorquez M, Kamat PV. Photophysical and photochemical aspects of coupled semiconductors: charge-transfer processes in colloidal cadmium sulfide-titania and cadmium sulfide-silver(I) iodide systems. *J Phys Chem*. 1990;94:6435–6440.
5. Zhang ZJ, Wang WZ, Yin WZ, Shang M, Wang L, Sun SM. Inducing photocatalysis by visible light beyond the absorption edge: effect of upconversion agent on the photocatalytic activity of Bi_2WO_6. *Appl Catal B*. 2010;10:68–73.
6. Vijayan BK, Dimitrijevic NM, Wu JS, Gray KA. The effects of Pt doping on the structure and visible light photoactivity of titania nanotubes. *J Phys Chem C*. 2010;114:21262–21269.
7. Shu X, He J, Chen D. Visible-light-induced photocatalyst based on nickel titanate nanoparticles. *Ind Eng Chem Res*. 2008;47:4750–4753.
8. Novoselov KS, Geim AK, Morozov SV, Jiang D, Zhang Y, Dubonos SV, Grigorieva IV, Firsov AA. Electric field effect in atomically thin carbon films. *Science*. 2004;306:666–669.
9. Geim AK. Graphene: status and prospects. *Science*. 2009;324:1530–1534.
10. Chen S, Zhu J, Wang X. From graphene to metal oxide nanolamellas: a phenomenon of morphology transmission. *ACS Nano*. 2010;4: 6212–6218.
11. Li YM, Lv XJ, Lu J, Li JH. Preparation of SnO_2-nanocrystal/graphene-nanosheets composites and their lithium storage ability. *J Phys Chem C*. 2010;114:21770–21774.
12. Akhavan O. Graphene nanomesh by ZnO nanorod photocatalysts. *ACS Nano*. 2010;4:4174–4180.
13. Novoselov KS, Geim AK, Morozov SV, Jiang D, Katsnelson MI, Grigorieva IV, Dubonos SV, Firsov AA. Two-dimensional gas of massless dirac fermions in graphene. *Nature*. 2005;438:197–200.
14. Sakamoto J, van Heijst J, Lukin O, Schlüter AD. Two-dimensional polymers: just a dream of synthetic chemists? *Angew Chem Int Ed*. 2009;48:1030–1069.
15. Burghard M, Klauk H, Kern K. Carbon-based field-effect transistors for nanoelectronics. *Adv Mater*. 2009;21:2586–2600.
16. Xu C, Wang X, Zhu J. Graphene-metal particle nanocomposites. *J Phys Chem C*. 2008;112:19841–19845.
17. Zhang H, Lv X, Li Y, Wang Y, Li J. P25-graphene composite as a high performance photocatalyst. *ACS Nano*. 2010;4:380–386.
18. Williams G, Seger B, Kamat PV. TiO_2-graphene nanocomposites: uv-assisted photocatalytic reduction of graphene oxide. *ACS Nano*. 2008;2:1487–1491.
19. Zhang Y, Tang ZR, Fu X, Xu YJ. TiO_2-graphene nanocomposites for gas-phase photocatalytic degradation of volatile aromatic pollutant: Is TiO_2-graphene truly different from other TiO_2-carbon composite materials? *ACS Nano*. 2010;4:7303–7314.
20. Yoo D H, Tran VC, Pham VH, Chung JS, Khoa NT, Kim EJ, Hahn SH. Enhanced photocatalytic activity of graphene oxide decorated on tio_2 films under uv and visible irradiation. *Curr Appl Phys*. 2011;11:805–808.
21. Akhavan O. Photocatalytic reduction of graphene oxides hybridized by zno nanoparticles in ethanol. *Carbon*. 2011;49:11–18.
22. Xu TG, Zhang LW, Cheng HY, Zhu YF. Significantly enhanced photocatalytic performance of zno via graphene hybridization and the mechanism study. *Appl Catal B*. 2011;101:382–387.
23. Shylesh S, Schunemann V, Thiel WR. Magnetically separable nanocatalysts: bridges between homogeneous and heterogeneous catalysis. *Angew Chem Int*. 2010;49:3428–3459.
24. Kinemuchi Y, Ishizaka K, Suematsu H, Jiang WH, Yatsui K. Magnetic properties of nanosize $nife_2o_4$ particles synthesized by pulsed wire discharge. *Thin Solid Films*. 2002;407:109–113.
25. Chung YS, Park SB, Kang DW. Magnetically separable titania-coated nickel ferrite photocatalyst. *Mater Chem Phys*. 2004;86:375–381.
26. Balaji S, Selvan RK, Berchmans LJ, Angappan S, Subramanian K, Augustin CO. Combustion synthesis and characterization of Sn^{4+} substituted nanocrystalline $NiFe_2O_4$. *Mater Sci Eng B*. 2005;119: 119–124.
27. Fu YS, Wang X. Magnetically separable $ZnFe_2O_4$-graphene catalyst and its high photocatalytic performance under visible light irradiation. *Ind Eng Chem Res*. 2011;50:7210–7218.
28. Hummers WS, Offeman RE. Preparation of graphitic oxide. *J Am Chem Soc*. 1958;80:1339–1339.
29. Wang H, Hao Q, Yang X, Lu L, Wang X. Effect of graphene oxide on the properties of its composite with polyaniline. *ACS Appl Mater Interfaces*. 2010;2:821–828.
30. Chen L, Dai H, Shen Y, Bai J. Size-controlled synthesis and magnetic properties of $nife_2o_4$ hollow nanospheres via a gel-assistant hydrothermal route. *J Alloys Comp*. 2010;491:L33–L38.

31. Nethravathi C, Nisha T, Ravishankar N, Shivakumara C, Rajamathi M. Graphene-nanocrystalline metal sulphide composites produced by a one-pot reaction starting from graphite oxide. *Carbon*. 2009;47: 2054–2059.
32. Bourlinos AB, Gournis D, Petridis D, Szabo T, Szeri A, Dekany I. Graphite oxide: chemical reduction to graphite and surface modification with primary aliphatic amines and amino acids. *Langmuir*. 2003;19:6050–6055.
33. Jeong HK, Lee YP, Lahaye RJWE, Park MH, An KH, Kim IJ, Yang CW, Park CY, Ruoff RS, Lee YH. Evidence of Graphitic AB stacking order of graphite oxides. *J Am Chem Soc*. 2008;130:1362–1366.
34. Guin D, Baruwati B, Manorama SV. Pd on amine-terminated ferrite nanoparticles: a complete magnetically recoverable facile catalyst for hydrogenation reactions. *Org Lett*. 2007;9:1419–1421.
35. Zhu ZR, Li XY, Zhao QD, Li H, Shen Y, Chen GH. Porous "brick-like" $NiFe_2O_4$ nanocrystals loaded with Ag species towards effective degradation of toluene. *Chem Eng J*. 2010;165:64–70.
36. Vasu KS, Chakraborty B, Sampath S, Sood AK. Probing top-gated field effect transistor of reduced graphene oxide monolayer made by dielectrophoresis. *Solid State Commun*. 2010;150:1295–1298.
37. Ray SC, Saha A, Basiruddin SK, Roy SS, Jana NR. Polyacrylate-coated graphene-oxide and graphene solution via chemical route for various biological application. diamond relat. *Materials*. 2011;20: 449–453.
38. Calizo I, Balandin AA, Bao W, Miao F, Lau CN. Temperature dependence of the raman spectra of graphene and graphene multilayers. *Nano Lett*. 2007;7:2645–2649.
39. Ferrari AC, Meyer JC, Scardaci V, Casiraghi C, Lazzeri M, Mauri F, Piscanec S, Jiang D, Novoselov KS, Roth S, Geim AK. Raman spectrum of graphene and graphene layers. *Phys Rev Lett*. 2006;97: 187401.
40. Iliev MN, Mazumdar D, Ma JX, Gupta A, Rigato F, Fontcuberta J. Monitoring B-site ordering and strain relaxation in $nife_2o_4$ epitaxial films by polarized raman spectroscopy. *Phys Rev B*. 2011;83: 014108.
41. Zhang LY, Li HS, Guan HM, Zhu DC. Study on preparation of ultrafine $NiFe_2O_4$ particles by microemulsion method. *Adv Liq Cryst*. 2010;428:511–514.
42. Bao N, Li YA, Wei ZT, Yin GB, Niu JJ. Adsorption of dyes on hierarchical mesoporous tio_2 fibers and its enhanced photocatalytic properties. *J Phys Chem C*. 2011;115:5708–5719.
43. Xu Y, Langford CH. UV- or visible-light-induced degradation of x3b on tio_2 nanoparticles: the influence of adsorption. *Langmuir*. 2001;17:897–902.
44. Wang X, Zhi LJ, Mullen K. Conductive graphene electrodes for dye-sensitized solar cells. *Nano Lett*. 2008;8:323–327.
45. Wang YJ, Shi R, Lin J, Zhu YF. Significant photocatalytic enhancement in methylene blue degradation of TiO_2 photocatalysts via graphene-like carbon *in situ* hybridization. *Appl Catal B*. 2010;100: 179–183.

Manuscript received Sep. 11, 2011, and revision received Nov. 11, 2011.